

# Gyrokinetic simulations of effects of magnetic islands on microturbulence in KSTAR

Xishuo Wei<sup>1\*</sup>, Javier H Nicolau<sup>1</sup>, Gyungjin Choi<sup>1,2</sup>, Zhihong Lin<sup>1</sup>, Seong-Moo Yang<sup>3</sup>, SangKyeun Kim<sup>3,4</sup>, WooChang Lee<sup>5</sup>, Chen Zhao<sup>6</sup>, Tyler Cote<sup>6</sup>, JongKyu Park<sup>3,2</sup>, Dmitri Orlov<sup>7</sup>

1. University of California, Irvine, CA, United States of America
2. Seoul National University, Seoul, Republic of Korea
3. Princeton Plasma Physics Laboratory, Princeton, NJ, United States of America
4. Princeton University, Princeton, NJ, United States of America
5. Korea Institute of Fusion Energy, Daejeon, Republic of Korea
6. General Atomics, San Diego, CA, United States of America
7. University of California, San Diego, CA, United States of America

\*Email: xishuow@uci.edu

## Abstract

Gyrokinetic simulations are utilized to study effects of magnetic islands on the ion temperature gradient (ITG) turbulence in the KSTAR tokamak with resonant magnetic perturbations. Simulations show that the transport is controlled by the nonlinear interactions between the ITG turbulence and self-generated vortex flows and zonal flows, leading to an anisotropic structure of fluctuation and transport on the poloidal plane and in the toroidal direction. Magnetic islands greatly enhance turbulent transport of both particle and heat. The turbulent transport exhibits variations in the toroidal direction, with transport through the resonant layer near the island X-point being enhanced when the X-point is located at the outer mid-plane. A quantitative agreement is shown between simulations and KSTAR experiments in terms of time frequency and perpendicular wavevector spectrum.

## 1 Introduction

During the H-mode operation of tokamaks, type-I Edge Localized Modes (ELMs) generate transient energy bursts at the plasma boundary, which can degrade plasma confinement and cause erosion of plasma-facing materials. One promising technique to avoid or mitigate these instabilities is the application of Resonant Magnetic Perturbations (RMPs)[1], originally developed to control magnetohydrodynamic (MHD) instabilities near the resonant magnetic surfaces. By applying current to external coils surrounding the tokamak, magnetic perturbations with helicity matching the field lines at resonant surfaces are generated. The RMP control of ELM has been demonstrated on several tokamak devices, including DIII-D[2], JET[3], KSTAR[4], and EAST[5], and is also predicted to be effective in future devices like ITER[6]. ELM suppression via RMPs enables long-pulse, steady-state operations while maintaining high confinement parameters. For instance, a KSTAR discharge[7] with a normalized plasma kinetic pressure  $\beta_N \approx 3$  was sustained for 12 seconds with an effective fusion gain  $G > 0.4$  using an edge safety factor  $q_{95} = 4$ . However, RMPs can also cause undesirable side effects on turbulent transport, such as a reduction in plasma density at both the edge and core (density pump-out) and an increase in the power threshold required to access high confinement mode (H-mode)[4], [8]. Understanding the physics mechanism of these RMP effects on turbulent transport is crucial for optimizing RMP configurations to achieve better confinement and higher fusion gain during steady-state operations. A key aspect of this is understanding the impact of magnetic islands (MIs) induced by the RMPs on the turbulent transport.

The MIs can form through magnetic reconnection on the rational surfaces where rotational transform of the unperturbed magnetic fields matches the RMP helicity. Even small MIs can significantly alter flux surface topology and plasma transport[9]. The impacts of MIs on plasma behavior have been observed across various tokamak and stellarator devices[10], [11], [12], [13]. The reduction in the pressure gradient within the island region has been observed, accompanied by a decrease in the turbulence intensity. Strong electron temperature  $T_e$  fluctuations have been observed near the X-point of the islands while the fluctuations near the island O-point are reduced. Turbulence can spread into the island region via the X-point. Some experiments have shown a

1  
2  
3 potential positive role of MIs in the formation of internal transport barriers (ITBs)[10], [12]. Recent experiments  
4 on KSTAR have shown that the inhomogeneous turbulence surrounding the MIs is related to variations in the  
5 ExB flow shear near the O-point and X-point[14]. Theoretical studies have also explored various aspects of MI  
6 effects on neoclassical transport[15] and bootstrap current[16], vortex flow generation[17], [18], and the long-  
7 term evolution of MIs[19]. Additionally, resonant interactions between particle motion and MIs have been  
8 studied theoretically [20], [21]. Despite these advances, the multiscale interactions between MIs and turbulent  
9 transport remain unsolved theoretically. There is no first-principles theory that can self-consistently predict  
10 turbulent transport in the presence of MIs. Numerical simulations are needed to further investigate the detailed  
11 mechanisms responsible for confinement degradation and to elucidate the spatial characteristics of turbulent  
12 transport.  
13

14 Extensive numerical studies have been conducted to understand the effect of MI and 3D fields on turbulent  
15 transport. It has been demonstrated that the MIs can stabilize[22] and localize[23] the ion temperature gradient  
16 (ITG) modes. The generation of vortex flows by MIs in neoclassical tearing mode (NTM) simulations is  
17 examined in [24], which was complemented by the study of mechanism of turbulence suppression via vortex  
18 flows[25]. Additional research into mean flow generation by MIs has also been conducted[26], [27]. Several  
19 studies have also shown that MIs suppress turbulent transport within the island region[28], [29], identifying a  
20 critical island width necessary for transport reduction. This finding has been further corroborated by later  
21 gyrokinetic simulations, which also identified the role of island width in transport suppression[30]. The  
22 mechanism of turbulence spreading into the island region has been explored in [31] and [32]. More recently, the  
23 effects of neoclassical toroidal viscosity (NTV) have been examined, with a focus on density pump-out, and  
24 these results have been compared directly to experimental data.[33], [34] More interesting studies on the multi-  
25 scale interaction between evolutionary MIs and turbulence were highlighted in the review papers[35], [36].  
26

27 In addition to the aforementioned studies, the Gyrokinetic Toroidal Code (GTC)[37] has been extensively  
28 employed to investigate the effects of 3D magnetic fields from RMPs and the interaction between magnetic  
29 islands (MIs) and other modes. GTC has been verified for a wide range of physical phenomena across various  
30 devices, including tokamaks, stellarators[38], and field-reversed configurations (FRCs)[39], encompassing  
31 neoclassical transport [16], microturbulence[40], meso-scale Alfvén eigenmodes (AEs)[41], and macro-scale  
32 MHD modes[42]. The impact of MIs on profile flattening and linear ITG instability has been studied in [43].  
33 The simulation model for tearing modes (TMs) was developed and TM instability in both the resistive and  
34 collisionless limits was verified[44], [45]. Further studies examined the effects of MIs on bootstrap current due  
35 to profile flattening within the island region[16]. The influence of electron cyclotron current drive on the  
36 evolution of MIs was investigated[46], [47]. The effects of MIs on ITG turbulent transport and the interactions  
37 between turbulence and MIs was studied in [48], [49]. The drift-tearing modes[50], [51] and double tearing  
38 modes[52] has been simulated. The interaction between energetic particles (EPs) and islands induced by NTMs  
39 was explored in [53]. More recently, the effect of island width on zonal flow generation and turbulent transport  
40 in a simple model tokamak was analyzed[54]. The NTM simulation was verified with the modified Rutherford  
41 equation and studied the influence of finite Larmor radius effects on NTM instability was studied[55]. In addition  
42 to these studies, GTC has also been employed to investigate the effects of non-resonant RMP fields on turbulent  
43 transport and the generation of radial electric fields[56], [57], [58]. These simulations offer valuable insights  
44 into the complex interplay between MIs, turbulence, and RMP fields, advancing our understanding of plasma  
45 transport in fusion devices.  
46

47 In this work, we use the GTC simulation to study the effects of the MIs on the turbulent transport using a realistic  
48 geometry and profiles in an actual experiment, KSTAR long-pulse discharge #19118, which features a large  
49 magnetic island with a width of approximately 4 cm [59] generated by the RMP that suppresses the ELMs. We  
50 performed global, self-consistent GTC electrostatic simulations using gyrokinetic ions and drift kinetic electrons.  
51 Our simulations verified the presence of anisotropic turbulence structures and turbulence spreading in the  
52 poloidal plane, regulated by nonlinear interactions between turbulence, zonal flows, and vortex flows. Magnetic  
53 islands greatly enhance turbulent transport of both particle and heat. We also observed that turbulent transport  
54 exhibits variations in the toroidal direction, with transport through the resonant layer near the X-point being  
55 enhanced when the X-point is located at the outer mid-plane. Furthermore, we compared the features of  
56  
57  
58  
59  
60

turbulence between GTC simulations and experimental observations, finding good agreements regarding the magnetic island effect on time frequency and perpendicular wavevector spectrum. The variation of density fluctuation at O-point and X-point are also similar to previous DIII-D[60] and TEXT experiments[61]. This work enhances our understanding of turbulent transport in the presence of MIs and provides insights in improving the confinement in RMP experiments.

This paper is organized as follows: Section 2 describes the KSTAR experimental data, the gyrokinetic simulation model including magnetic islands, and the simulation settings. Section 3 presents the results of the turbulence simulations. Finally, a summary is provided in Section 4.

## 2 Simulation model and simulation settings

The experimental data of KSTAR discharge #19118 at  $t=2950\text{ms}$  is presented in Fig.1. The  $n=1$  RMP was applied at  $t=2400\text{ms}$  in the discharge, leading to the formation of the MI and the subsequent mode locking was observed at  $t=2800\text{ms}$ . At  $t=2950\text{ms}$ , the radial electron temperature profile exhibits a clear flattening effect near  $q=2$  surface. The  $q=2$  surface is located at  $\rho_t = 0.549$ , and the island region covers from  $\rho_t = 0.42$  to  $\rho_t = 0.65$  in the neighbor of O-points. Here,  $\rho_t \equiv \sqrt{\psi_N}$  and  $\psi_N$  is the normalized toroidal magnetic flux. Consistently, the Electron Cyclotron Emission Imaging (ECEI) data reveals the  $(m,n)=(2,1)$  MI structure at the  $q=2$  surface. On the other hand, no clear flattening effect is observed in the electron density and ion temperature, possibly due to the large error in the measurements of these profiles. In the simulations, we consider a single ion species (Deuterium) and assume the equilibrium ion density  $n_{i0}$  to be identical to electron density  $n_{e0}$ .

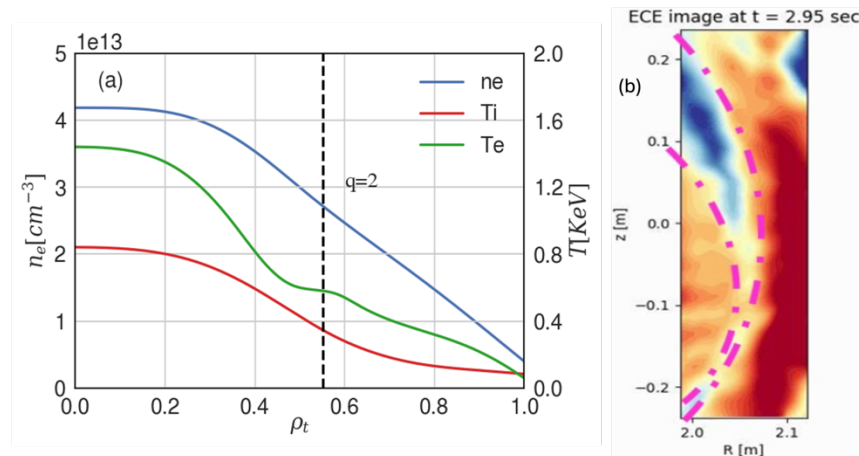


Figure 1 (a) The radial profiles of electron temperature, electron density, and ion temperature of KSTAR shot #19118 at  $t=2.95\text{s}$ . The RMP has been turned on and the MI has been formed.  $n_i$  is assumed to be identical to  $n_e$ . (b) The temperature fluctuations on the  $R$ - $Z$  poloidal plane measured by ECE imaging at  $t=2.95\text{s}$ . The two magenta curves show the separatrix of MI.

GTC employs gyrokinetic equations for both ions and electrons to simulate the low-frequency waves and the associated turbulent transport. The static magnetic field can be expressed as  $\mathbf{B} = \mathbf{B}_0 + \nabla \times (\alpha_{IS} \mathbf{B}_0)$ , where  $\mathbf{B}_0$  is the ambient magnetic field, and  $\delta \mathbf{B}_{IS} \equiv \nabla \times (\alpha_{IS} \mathbf{B}_0)$  is the magnetic field induced by the static MI. Both of  $\mathbf{B}_0$  and  $\alpha_{IS}$  in the Boozer coordinate system are solved by M3D-C1 code[62] based on the KSTAR experimental data. The shape of the island field is shown in Fig.2. The left panel illustrates that the maximum amplitude of  $\alpha_{IS}$  is located at the X-points and the O-points. The right panel presents the Poincare plot electron guiding center orbit at the  $\zeta = \pi$  plane, with the X-point situated at the outer mid-plane. The electron motion is confined to the constant perturbed flux  $\psi_h$  surfaces, clearly displaying the  $(2,1)$  island structure since the electron guiding center orbit width is very small compared with the MI size. the helical flux  $\psi_h$  can be approximately calculated from  $\psi_h \approx \psi_{p0} - \psi_{t0}/2 - \alpha_{IS}g$  to represent the perturbed flux surfaces near  $q=2$  surface, where the  $\psi_{p0}$  and  $\psi_{t0}$  are the unperturbed poloidal and toroidal flux functions, and  $g$  is the poloidal current in the covariant Boozer representation ambient magnetic field  $\mathbf{B}_0 = \delta \nabla \psi_0 + I \nabla \theta + g \nabla \zeta$ .

In this work, the simulations are conducted in the plasma frame, assuming a time scale shorter than the island evolution time. Consequently, we consider the perturbed (2,1) magnetic field  $\delta\mathbf{B}_{IS}$  as part of the equilibrium field and focus on the electrostatic turbulence transport. The particle dynamics are described by the gyrokinetic equation with the parallel symplectic representation of the modern gyrokinetic model. The distribution function  $f_s$  of species ‘s’ (ions or electrons) follows the collisionless gyrokinetic Vlasov equation,

$$(L_0 + L_{\delta B} + \delta L)f_s = 0, \quad (1)$$

where

$$L_0 = \frac{\partial}{\partial t} - \frac{\mu}{m_s} \frac{\mathbf{B}_0^*}{B_{0\parallel}^*} \cdot \nabla B_0 \frac{\partial}{\partial v_{\parallel}} + v_{\parallel} \frac{\mathbf{B}_0^*}{B_{0\parallel}^*} \cdot \nabla + \frac{\mu}{Z_s B_{0\parallel}^*} \mathbf{b}_0 \times \nabla B_0 \cdot \nabla, \quad (2)$$

$$L_{\delta B} = \left( \frac{B_{0\parallel}^*}{B_{\parallel}^*} - 1 \right) L_0 + v_{\parallel} \frac{\delta\mathbf{B}_{IS}}{B_{\parallel}^*} \cdot \nabla - \frac{\mu}{m_s} \frac{\delta\mathbf{B}_{IS}}{B_{\parallel}^*} \cdot \nabla B \frac{\partial}{\partial v_{\parallel}}, \quad (3)$$

$$\delta L = \frac{(\mathbf{b}_0 + \delta\mathbf{B}_{IS}/B_0) \times \nabla \delta\bar{\phi}}{B_{\parallel}^*} \cdot \nabla - \frac{1}{m_s} \frac{\mathbf{B}_0 + \delta\mathbf{B}_{IS}}{B_{\parallel}^*} \cdot Z_s \nabla \delta\bar{\phi} \frac{\partial}{\partial v_{\parallel}} - v_{\parallel} \frac{\nabla \times (\mathbf{b}_0 + \delta\mathbf{B}_{IS}/B_0) \cdot \nabla \delta\bar{\phi}}{B_{\parallel}^*} \frac{\partial}{\partial v_{\parallel}}, \quad (4)$$

Where  $\mathbf{b}_0 = \mathbf{B}_0/B_0$ ,  $\mathbf{B}_0^* = \mathbf{B}_0 + m_s v_{\parallel} \nabla \times \mathbf{b}_0/Z_s$ ,  $B_{0\parallel}^* = \mathbf{B}_0^* \cdot \mathbf{b}_0$ ,  $B_{\parallel}^* = B + (m_s v_{\parallel} \nabla \times \mathbf{b}_0/Z_s) \cdot \mathbf{b}_0$ .  $m_s$  and  $Z_s$  denote the particle mass and charge.  $\delta\bar{\phi}$  is the gyroaveraged potential for ions, and we ignore the finite Larmor radius effect for electrons due to small electron gyroradius (i.e., by using electron drift kinetic equation). The  $\delta f$  method is used in this work to reduce the numerical noise. The equilibrium distribution is defined by  $L_0 F_{s0} = 0$ , where  $F_{s0}$  is the neoclassical solution in the absence of the MI. And  $\delta f_s$  is solved from

$$(L_0 + L_{\delta B} + \delta L)\delta f_s = -(L_{\delta B} + \delta L)F_{s0}, \quad (5)$$

where we use the local Maxwellian to approximate  $F_{s0}$  in the  $\delta f_s$  equation. The gyrokinetic Poisson equation is used to close the system in the electrostatic simulations.[63], [64]

$$\frac{Z_i^2 n_{0i}}{T_{0i}} (\delta\phi - \delta\bar{\phi}) = Z_i \delta\bar{n}_i + Z_e \delta n_e, \quad (6)$$

Where  $\delta\bar{n}_i$  and  $\delta n_e$  are the gyroaveraged guiding center density of ions and electrons. The detailed derivation of the simulation model can be seen in[48]. In simulations without magnetic islands (MIs), it is common practice to solve the electron adiabatic and non-adiabatic responses separately from drift kinetic equation using an iterative method[65], [66]. However, when MIs are present, the situation becomes more complex because electrons move along the perturbed magnetic field lines. In this case, distinguishing between adiabatic and non-adiabatic responses requires separating the electrostatic potential perturbation ( $\delta\phi$ ) into ‘zonal’ and ‘non-zonal’ components. This separation is based on whether the local parallel wavenumber ( $k_{\parallel}$ ) is zero, meaning the parallel derivative along the perturbed magnetic field lines is zero. This process is numerically challenging, as it involves complex field-line-following calculations. To avoid these complications, we solve  $\delta\phi$  as a whole, without splitting it into zonal and non-zonal components. As a result, the electron distribution function  $\delta f_e$  must also be solved in its entirety using the complete drift-kinetic equation, rather than separating the adiabatic and non-adiabatic components.

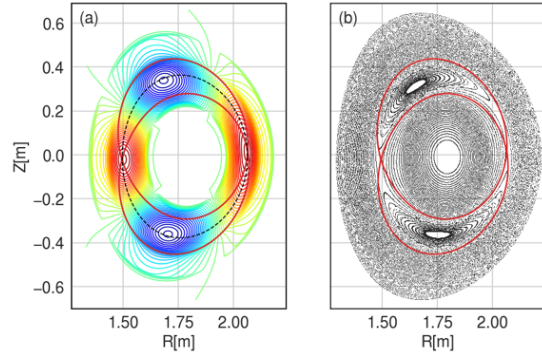


Figure 2 (a) The perturbed magnetic field potential  $\alpha_{1S}$  at  $\zeta = \pi$  poloidal plane. (b) the Poincare plot of electron guiding center orbits at  $\zeta = \pi$  poloidal plane. The red solid lines are the constant  $\psi_h$  contour that shows the island separatrix. The dashed line stands for  $q=2$  surface. The same notations are used for the other figures as well.

### 3 simulation results

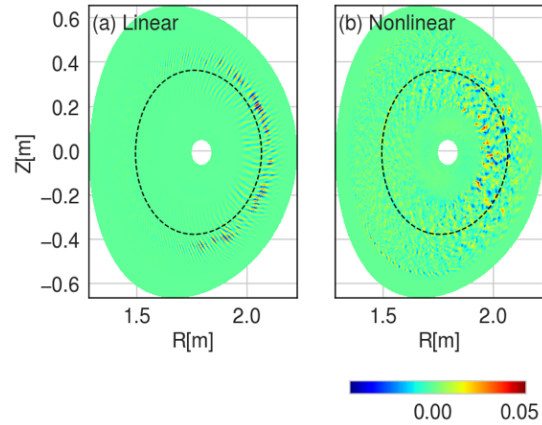


Figure 3 Electrostatic potential  $e\phi/T_e$  on poloidal plane in the (a)linear and (b)nonlinear stage of the ITG instability without magnetic island. The color scale for nonlinear potential is shown under panel(b).

To identify the dominant driftwave instability and to delineate the effect of MI, we first exclude the MI field  $\delta\mathbf{B}_{IS}$  from the self-consistent turbulence simulation and identify the ion temperature gradient (ITG) mode as the dominant instability. The most unstable eigenmode has  $n=75$  and  $m \approx 165$ ,  $k_\theta \rho_i \sim 0.55$  with the largest amplitude located at the  $q=2.2$  surface (See Fig.3). The linear growth rate and frequency are  $\gamma = 6.6 \times 10^4 s^{-1}$  and  $\omega = 3.9 \times 10^4 s^{-1}$ , respectively. In the nonlinear stage, small isotropic eddies form due to the shearing effects of zonal flows. The turbulence fluctuation spreads inward and covers the  $q = 2$  region. The averaged heat conductivity between  $\rho_t = 0.37$  and  $\rho_t = 0.71$  of ions and electrons in nonlinear stage are  $\chi_i \approx 2.8 m^2/s$ ,  $\chi_e \approx 2.1 m^2/s$ , respectively.

We perform the simulation with MI with two stages, the Monte-Carlo stage for pressure relaxation (i.e., only  $n=1$  mode) due to the static MI, and the self-consistent turbulence simulation (i.e., all  $n$  modes). Note that the initial density profile in Fig. 1 is not flattened within the island region. If we start the simulation with both MI profile relaxation and self-consistent turbulence, the long time-scale pressure flattening effect emerges due to the equilibrium term  $-\nu_{\parallel} \frac{\delta\mathbf{B}_{IS}}{B_{\parallel}^*} \cdot \nabla F_{S0}$  in the RHS of Equation (5). Because of the different flattening of ions and electrons, the non-oscillating charge difference will be created, and consequently an unphysically large electric field is artificially created. This problem is solved by first finding the appropriate initial value of  $\delta f$  using Monte-Carlo simulation.

### 3.1 Monte-Carlo simulation

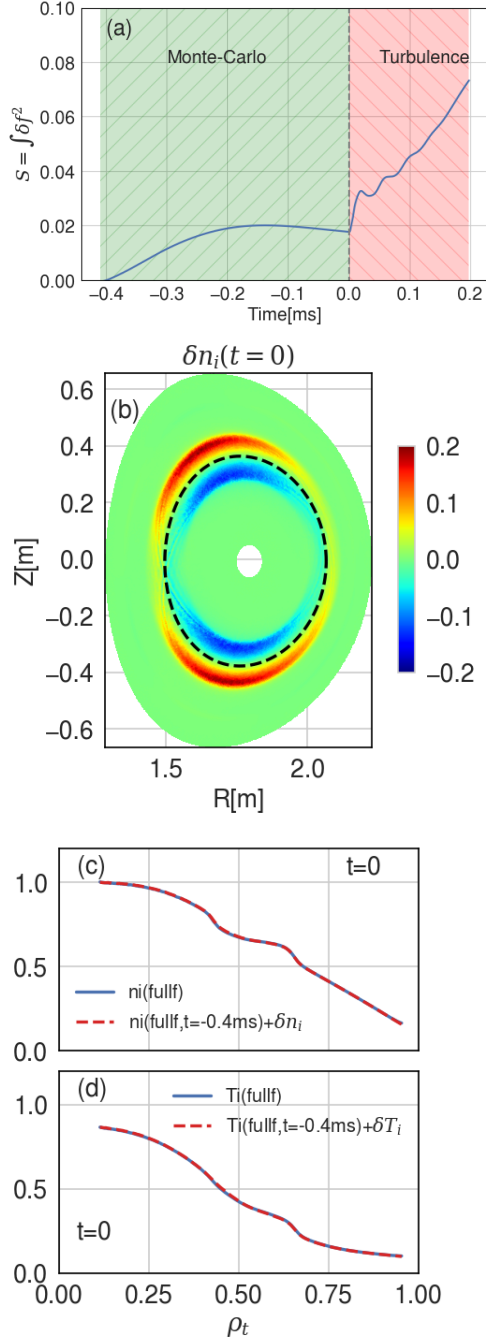


Figure 4 (a) The time history of particle entropy. The Monte-Carlo stage is from  $t=-0.4$ ms to  $t=0$ , and the turbulence stage is from  $t=0$  to  $t=0.2$ ms. (b)(c)(d) The flattened profiles at  $t=0$ , after the finish of Monte-Carlo stage. (b)  $\delta n_i$  on the  $\zeta = \pi$  poloidal plane. (c) Radial ion density profile v.s.  $\rho_t$ , normalized by  $n_e$  on axis. (d) Radial ion temperature profile v.s.  $\rho_t$ , normalized by  $T_e$  on axis. In (c) and (d) the two curves coincide with each other.

In the Monte-Carlo simulation,  $\delta\phi$  is forced to be 0. We solve the perturbed ion distribution function from

$$(L_0 + L_{\delta B})\delta f_{iMC} = -L_{\delta B}F_{i0}, \quad (7)$$

and ions are redistributed spatially under the effect of  $\delta\mathbf{B}_{IS}$ . Fig. 4(a) shows the time evolution of the entropy, defined as  $S_i = \int \delta f_i^2 d^3\mathbf{v} d^3\mathbf{x}$ , which indicates the deviation from the initial equilibrium  $F_{i0}$ . The Monte-Carlo

ion simulation is stopped after or 0.4 ms when the entropy reaches its maximum value. The ion profile at the end of the simulation is shown in Fig. 4. In the Monte-Carlo stage (from -0.4 ms to 0 ms), the  $S_i$  increases due to flattening effect and eventually reaches a steady value. And in the turbulence stage,  $S_i$  continues to increase with the perturbed electric field. The turbulence simulation ends at  $t = 0.2$  ms, before the emergence of numerical instability. The density and temperature flattening near  $q=2$  surface can be observed in Fig.4(c) and Fig.4(d). Here, the profile can be calculated using the  $\delta f$  or full- $f$  approach and they agree with each other. Then we take  $\delta f_{iMC}$  as the initial value of both delta  $\delta f_i$  and  $\delta f_e$  and start the turbulence simulation by solving Equation (5). Since the  $-L_{\delta B} F_{i0}$  term will be cancelled with the initial value of LHS in (5), there is no long time-scale evolution of  $\delta f_s$  due to MI and the quasi-neutrality condition is satisfied.

### 3.2 Turbulence simulation with MI

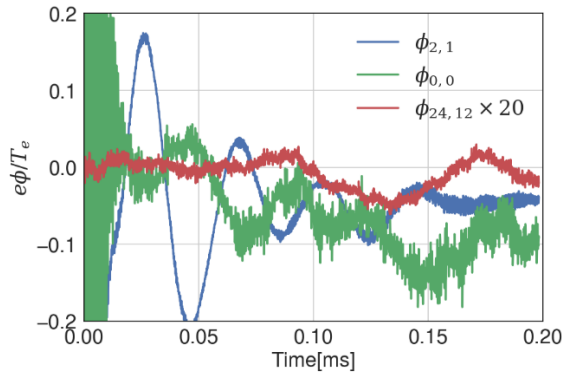


Figure 5 Time history of  $\phi$  in the simulation with MI at  $q=2$  surface.  $\phi_{00}$  is the zonal component.  $\phi_{2,1}$  is the vortex flow component.  $\phi_{24,12}$  is the dominant turbulence fluctuation at  $q=2$  surface.  $\phi_{24,12}$  has been amplified by 20 times in the plot for visibility.

Fig.5 shows the evolution of electrostatic potential  $\phi$ . Due to the large perturbation from the Monte-Carlo simulation, a large particle noise in  $\phi_{00}$  and  $\phi_{2,1}$  is created at the beginning of turbulence simulation (but decreases rapidly), and simulation soon enters the nonlinear stage. The evolution of  $\phi$  is dominant by the zonal component  $\phi_{00}$  and the vortex flow  $\phi_{2,1}$ . These two components are linearly coupled through the (2,1) magnetic field of the MI, and oscillate at a frequency  $\omega = 1.7 C_s/R_0$ , which is slightly lower than the theoretical GAM frequency  $\omega_{GAM} \approx 2.1 C_s/R_0$ . The dominant harmonic of turbulence is  $m = 24, n = 12$  at  $q = 2$  surface, and the oscillation of  $\phi_{24,12}$  is much slower than ITG frequency in the case without MI and has a much lower amplitude compared to the vortex flow. Further analysis shows the oscillation of the real and imaginary parts of  $\phi_{2,1}$  are in phase, which means that the vortex mode is a standing wave, with antinodes located at the X-points and O-points of the islands.

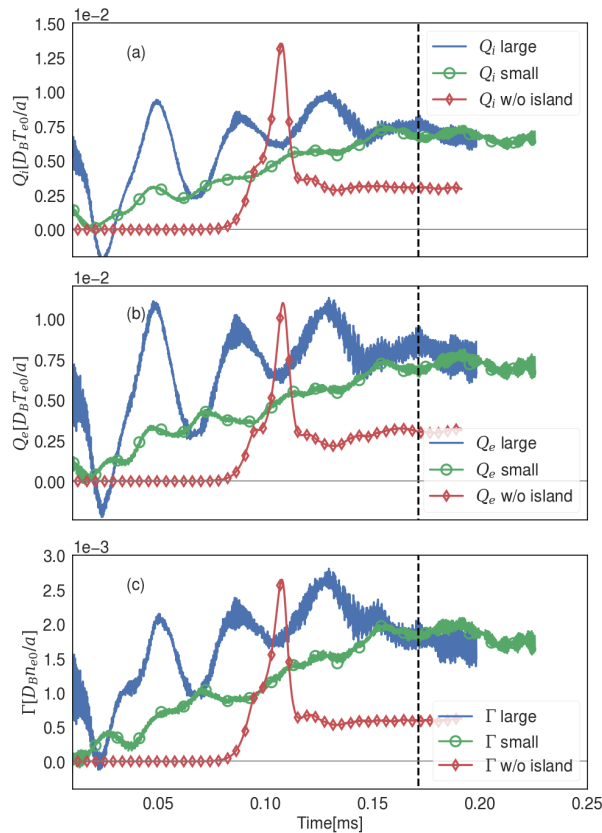


Figure 6 The time history of Ion heat flux  $Q_i$  (panel a), electron heat flux  $Q_e$  (panel b), and particle flux  $\Gamma$  (panel c).  $\Gamma$  is defined as the half of ion and electron particle flux summation,  $\Gamma \equiv (\Gamma_i + \Gamma_e)/2$ . The vertical line corresponds to and  $t=0.17\text{ms}$  for latter analysis.  $Q$  and  $\Gamma$  are normalized by  $D_B T_{e0}/a$  and  $D_B n_{e0}/a$ , respectively.  $D_B = T_{e0}/eB_0$  is the Bohm unit.  $n_{e0}$  and  $T_{e0}$  stand for the electron density and temperature on axis.  $a$  is the minor radius at plasma wall.

The time history of volume averaged particle and heat fluxes are plotted in Fig. 6. The particle flux is calculated by  $\Gamma_s = \int d^3v v_r \delta f_s$ , and the heat flux is calculated by  $Q_s = \int d^3v \left( \frac{1}{2} m v^2 - \frac{3}{2} T_s \right) v_r \delta f_s / n_{0s}$ , where  $v_r$  is the radial  $E \times B$  velocity, and  $n_{0s}$  is the equilibrium density for species ‘s’. In Fig. 6 the volume average is taken between  $\rho_t = 0.35$  and  $\rho_t = 0.72$  for all cases. An additional simulation with  $\alpha'_{IS} = \alpha_{IS}/2$  was conducted to examine the effect of island size on transport. We refer the simulation with standard  $\alpha_{IS}$  as the ‘large island case’ and the one with  $\alpha'_{IS}$  as the ‘small island case’. The transport is clearly modulated by the vortex mode frequency, which is close to the GAM frequency. However, the oscillation is less significant in the small island case due to the weaker vortex mode and smaller island size. In the simulations without island,  $Q_i$  and  $Q_e$  show a clear linear growth and nonlinear saturation stage. In contrast, in the simulations with islands, the transport level continuously oscillates and increases without a linear growth phase. When the GAM and vortex mode oscillation damps to the residual level, the transport also reaches a steady value. The MI enhances  $Q_i$  and  $Q_e$  by a factor 3. Although the oscillation amplitude and the rate of increase of heat transport over time are smaller in the small island case compared to the large island case, the final steady transport level is similar for both cases. The temporal evolution of particle flux  $\Gamma$  in Fig.6(c) is similar to heat flux. But importantly, it shows the enhancement of  $\Gamma$  by MI, which is consistent with the density pump-out result in RMP experiments.

### 3.3 Turbulence regulation by zonal flows and vortex flows

The instantaneous Er shearing rate of zonal flows can be calculated as  $\omega_s = \partial^2 \phi_{00} / \partial \psi^2 \times R_0^2 B_\theta^2 / B_0$ , which assumes turbulence eddies are isotropic in radial and poloidal direction. The  $E_r$  shearing rate averaged over unperturbed flux surfaces from simulation with and without MI are presented in Fig.7(a) and Fig.7(b) as



functions of time and radial location. The zonal flow shearing rate has barriers at the island separatrix, particularly at the outer one. Within the island region ( $0.42 < \rho_t < 0.65$ ),  $\omega_s$  shows minimal radial dependence and it exhibits damping while oscillating at the GAM frequency. The damping is also observed in the  $\phi_{2,1}$  vortex mode in Fig.5. The zonal flow shearing rate within the island region eventually reaches to a residual level  $|\omega|_s \approx 1.6 \times 10^5 \text{ s}^{-1}$  which is significantly lower compared to the no-island case, where  $|\omega|_{s,nois} \approx 1.5 \times 10^6 \text{ s}^{-1}$ . However, it is important to note that the effective shearing rate in the no-island case can be reduced due to the finite oscillation frequency of  $\omega_s$  [67]. The relation between zonal flow shearing rate and transport can be seen in Fig. 8. The transport is lower where the shearing rate is large in both cases. And the MI has an enhancement for particle and heat flux at all radial locations.

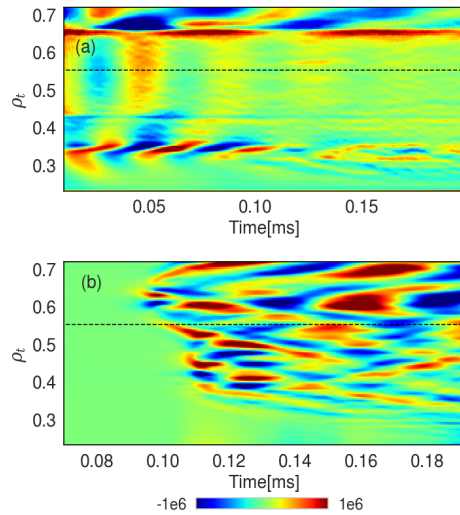


Figure 7 Zonal flow shearing rate  $\omega_s$  as function of simulation time and radial location. The unit of  $\omega_s$  is  $1/s$ . (a) With MI. (b) Without MI. The horizontal dashed line shows the  $q=2$  surface.

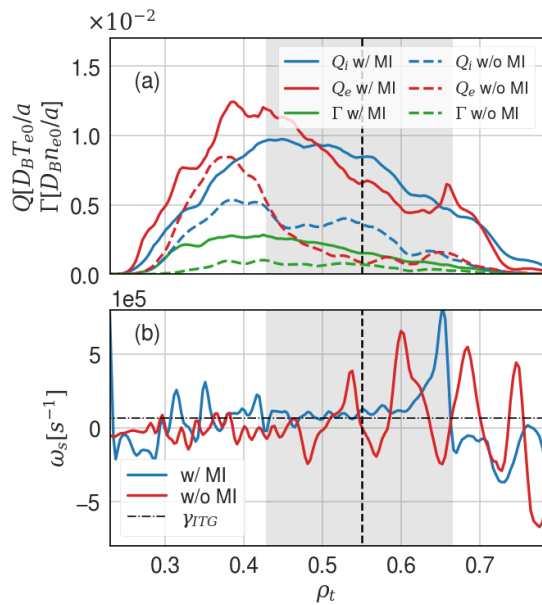


Figure 8 Time averaged radial profile of particle flux, heat flux, and zonal flow shearing rate  $\omega_s$ . Time window is  $[0.16, 0.20] \text{ ms}$  for case with MI, and  $[0.14, 0.17] \text{ ms}$  for case without MI.  $Q$  is normalized by  $D_B T_{e0}/a$ . The linear growth rate of ITG without island ( $\gamma = 6.6 \times 10^4 \text{ s}^{-1}$ ) is shown as the horizontal black dash line in panel (b). The gray shaded area shows the island region near O-points. The vertical dashed line shows the  $q=2$  surface.

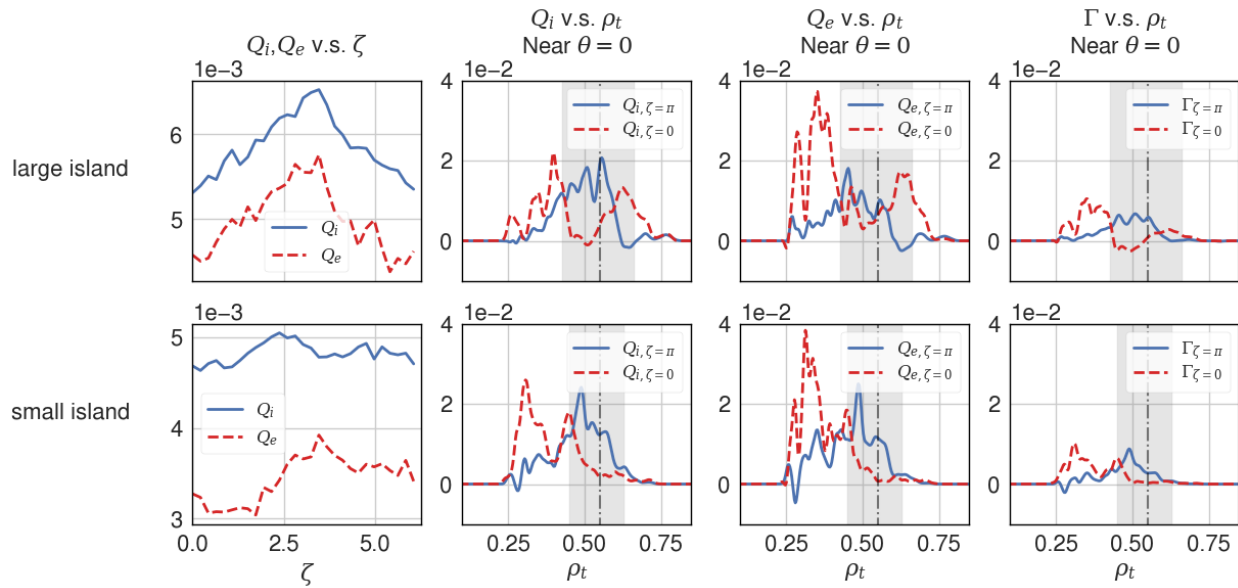


Figure 9  $Q_i$ ,  $Q_e$ , and  $\Gamma = (\Gamma_i + \Gamma_e)/2$  when  $t=0.171$  ms (labeled time step in Fig.6). the two rows correspond to the large island case and the small island case, respectively. (First column) Poloidal plane averaged  $Q_i$  and  $Q_e$  at different  $\zeta$  angle, the radial averaging is taken between  $\rho_t = 0.42$  and  $\rho_t = 0.65$  for large island case, and between  $\rho_t = 0.45$  and  $\rho_t = 0.62$  for small island case.  $\Gamma$  has a similar toroidal variance as  $Q$  and not shown in the first column. (Second, third, and fourth column)  $Q_i$ ,  $Q_e$ , and  $\Gamma$  averaged between  $\theta \in [-\pi/8, \pi/8]$ , when  $\zeta = 0$  (Near O-point) or  $\zeta = \pi$  (Near X-point). Shown as a function of  $\rho_t$ . Shaded area shows the island region near O-points, and the vertical dashed line shows  $q=2$  surface.  $Q$  and  $\Gamma$  are normalized by  $D_B T_{e0}/a$  and  $D_B n_{0e}/a$ , respectively.

To further examine effect of MI on the transport spatial structures, we plot the radial and toroidal variance of particle and heat transport in Fig.9. When  $t=0.171$  ms, the vortex flow damps to a residual level and the transport reaches steady level. In the first row, the first column indicates that  $Q_i$  and  $Q_e$  in the large island case exhibits a clear toroidal angle dependence. The radial dependence of  $Q$  and  $\Gamma$  near outer mid plane ( $\theta = 0$ ) are plotted in the next three columns, where we see the clear transport concentration at X-point, and the transport suppression at O-point. We should note that the toroidal dependence is not only due to the difference between O-point and X-point, but also due to the difference of X-points at  $\zeta = 0$  and  $\zeta = \pi$ . In the small island case (second row of Fig.9), the toroidal variance of transport is less clear. Although the transport is suppressed in the island region near O-point, the strong transport level is found at smaller  $\rho_t$ . Besides, the transport level near the X-points at  $\zeta = 0$  and  $\zeta = \pi$  is similar. Thus, the differences between poloidal planes at different  $\zeta$  angles is reduced.

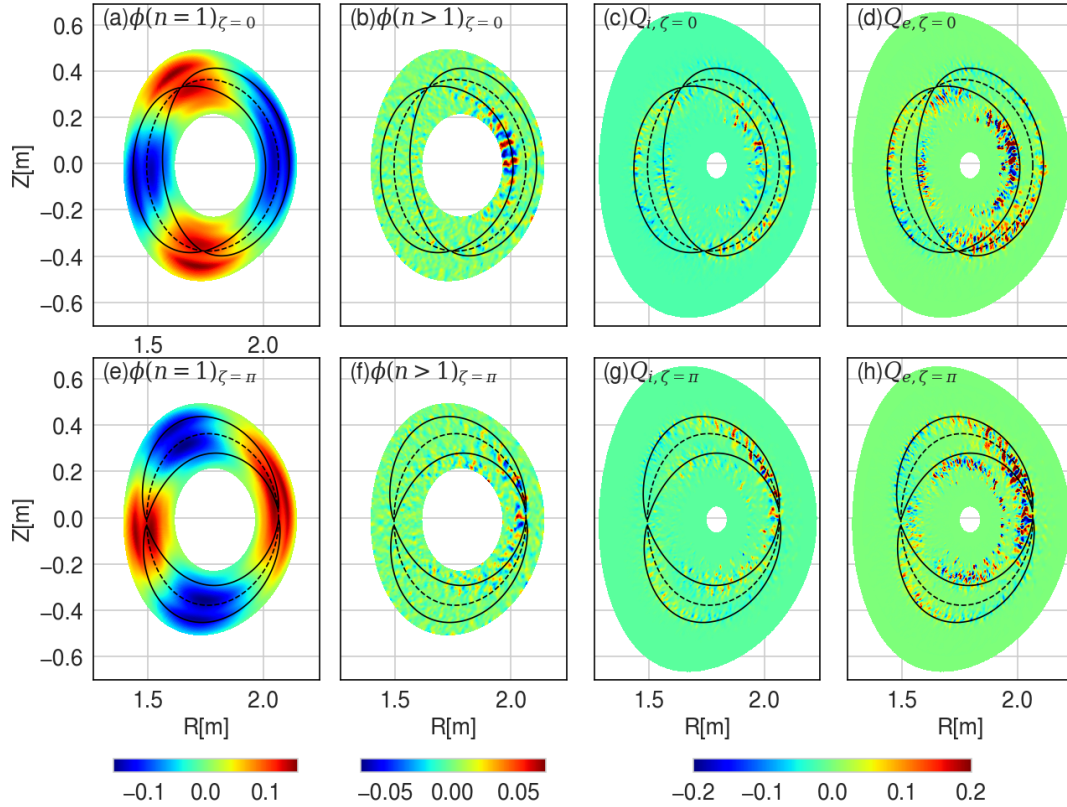


Figure 10 The electrostatic potential and heat flux at  $t=0.17\text{ms}$ . (a) and (e)  $\phi(n=1)$  component at  $\zeta=0$  and  $\zeta=\pi$ . (b) and (f) turbulence component of  $\phi$  at  $\zeta=0$  and  $\zeta=\pi$ ,  $\phi(n>1)=\phi-\phi_{00}-\phi(n=1)$ . (c) and (g) ion heat flux  $Q_i$  at  $\zeta=0$  and  $\zeta=\pi$ . (d) and (h) electron heat flux at  $\zeta=0$  and  $\zeta=\pi$ . The potential is normalized by  $T_{e0}/e$ , and the  $Q$  is normalized by  $D_B T_{e0}/a$ .

Interplays between vortex flows and turbulence are illustrated in Fig. 10, which shows the snapshots of vortex flow  $\phi(n=1)$  and turbulence component of potential  $\phi(n>1)$  and radial heat flux  $Q_i$  and  $Q_e$  during the turbulence simulation when  $t=0.17\text{ms}$ .  $\phi(n=1)$  simply rotates along the field line and structure does not depend on  $\zeta$  angle, while the different effect of MI at different toroidal angles is observed for turbulence fluctuation and associated transport. At  $\zeta=0$ , the O-point is located at mid-plane, and the potential fluctuation is maximum near the inner separatrix at the outer mid-plane ( $\theta=0$ ). The heat flux is mainly along the separatrix, especially at the region near X-points. This observation shows the effect from the vortex flow shear, which is qualitatively the same as the results in the analytical geometry[48], [54]. Compared to the analytical geometry, the simulations in KSTAR geometry show smaller eddy size, and at  $\zeta=0$  poloidal plane, the turbulence fluctuation of  $\phi$  near X-points is not strong since it is not in the bad curvature region. At  $\zeta=\pi$ , the maximum values of potential fluctuation and the heat flux are found near the X-point at  $\theta=0$ . Comparing with the poloidal structure of  $\phi$  at earlier time points (not shown here) in the simulation, the turbulence spreading into the island region through X-point can be clearly observed near the X-point at  $\theta=0$ . Compared to the  $\zeta=0$  plane, the turbulence amplitude is larger near this X-point, since the ITG turbulence drive is stronger at outer mid-plane (see Fig.3 (b)). Consequently, the turbulent transport across  $q=2$  surface is also stronger at  $\zeta=\pi$  than  $\zeta=0$ . This observation is consistent with the 1-dimensional analysis in Fig.9.

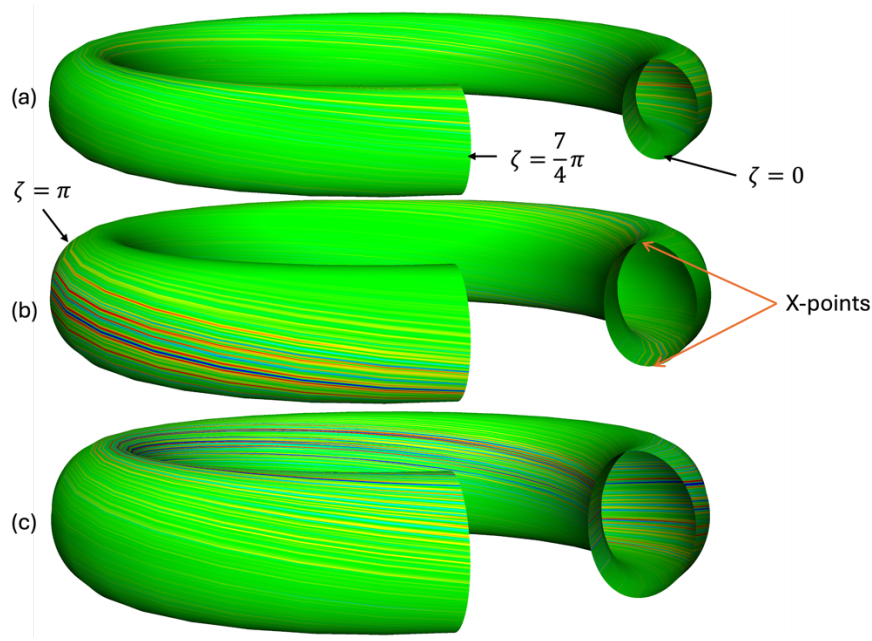


Figure 11  $Q_i$  on different flux surfaces when  $t=0.17ms$ . (a)  $\rho_t = 0.42$ (near inner separatrix) (b)  $\rho_t = 0.55$  ( $q=2$  surface) (c)  $\rho_t = 0.65$  (near outer separatrix).  $Q_i$  is normalized by  $D_B T_{e0}/a$ . The torus from  $\zeta = 0$  to  $\zeta = 7/4 \pi$  is shown. The two X-points at  $\zeta = 0$  are labeled in panel(b).

The vortex flow effect on the transport can also be clearly seen from a 3-D plot in Fig. 11. Three flux surfaces are selected with  $q=1.69$ ,  $q=2$ , and  $q=2.33$ , and  $Q_i$  are plotted on these surfaces. Here, the  $q = 1.69$  and  $q = 2.33$  surfaces are selected to be tangent to the inner and outer separatrix, respectively. In Fig. 11(a) and Fig. 11(c), the  $\theta$  value corresponding to the maximum  $Q_i$  at  $q = 1.69$  and  $q = 2.33$  surfaces varies toroidally, matching the phase of island, but the poloidally averaged amplitude of  $Q_i$  does not depend on the toroidal angle significantly. In Fig. 11(b), the maximum region for  $Q_i$  at  $q = 2$  appears only near  $\zeta = \pi$  and  $\theta = 0$ , which is in consistency with the toroidal varying  $Q$  in Fig. 10. This again shows the transport is easier to cross the  $q = 2$  surface near  $\zeta = \pi$ . Thus, the toroidal variance of the fluctuation and transport property is created in a tokamak with MIs.

### 3.4 Comparison with experiments

The ion and electron perturbed densities fluctuations at the  $\zeta = \pi$  poloidal plane is shown in Fig. 12. The similarity in densities between the two species demonstrates the maintenance of quasi-neutrality condition during the simulation. We measured the density fluctuation level at  $q=2$  surface, defined by  $\delta\tilde{n} = \delta n - \delta n_{00} - \delta n_{2,1}$ , and found the fluctuation is suppressed at the O-points. This fluctuation regulation effect from the MI is consistent with previous observations in TEXT[61] and DIII-D[60] experiments. Additionally, we show the two X-points are not equivalent, and the fluctuation is only maximum when  $\theta = 0$ .

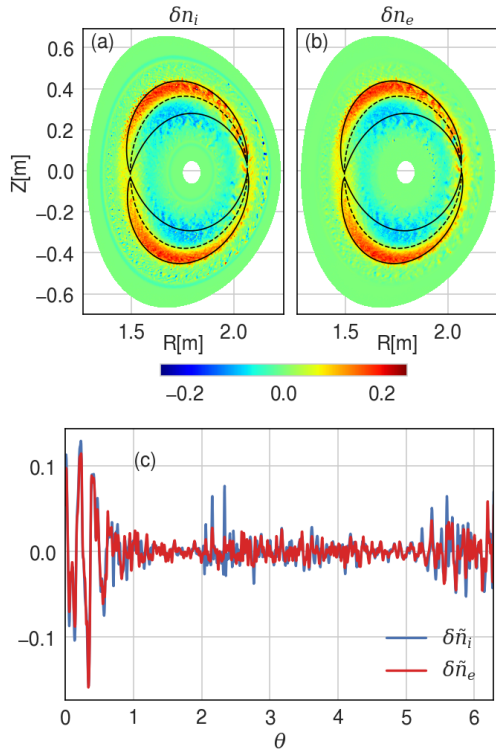


Figure 12 The density fluctuations on the  $\zeta = \pi$  poloidal plane of ions(a) and electrons(b) when  $t=0.17$ ms. (c) The density fluctuations at  $q=2$  surface dependence on poloidal angle. Density is normalized to the electron density on magnetic axis.

Fig.13 compares the frequency spectrum of the turbulence between KSTAR experiments and GTC simulations. In the KSTAR discharge #19115 with RMP suppressing ELM, the turbulence fluctuation frequency near the X-point were measured using Microwave Imaging Reflectometry (MIR)[68], [69]. The experimental conditions are similar to those in the simulated discharge #19118[59]. The MIR measurements were recorded at two time points:  $t = 2.8$  s (before RMP and mode locking), labeled as ‘MIR w/o island’, and  $t=3.05$ s (after RMP, with mode locking) labeled as ‘MIR w/ island’. The corresponding frequency spectrum from GTC simulations is obtained by conducting the Fourier transformation to the dominant turbulence harmonics. In Fig.13, the blue line represents the GTC simulation with the island, and the red line represents the simulation without the island. Prior to the RMP (orange line), a peak frequency at 150 kHz corresponds to the toroidal rotation frequency. After the formation of the magnetic island (MI), the mode becomes locked, and the peak frequency drops to 0. GTC simulations are performed in a rotating frame, the red line in Fig.13 is horizontally shifted by the toroidal rotation frequency for better visibility. A reduction of the width of the spectrum is observed in both experiments and simulations. The standard deviation of the frequency spectrum, which quantifies the width, was calculated and shows consistency between the experiments and simulations, as listed in Table 1. Note that GTC simulations exhibit a high-frequency tail, especially for the case with island, which is likely caused by numerical noise and the finite simulation time. Therefore, the frequency range was restricted in the calculation of the standard deviation: from -100 kHz to 100 kHz for the "with island" case, and from -200 kHz to 500 kHz for the "no island" case. It is worth noting that the MI effect on both the spectrum shape and the width agrees quantitatively between simulations and experiments, which is reported for the first time.

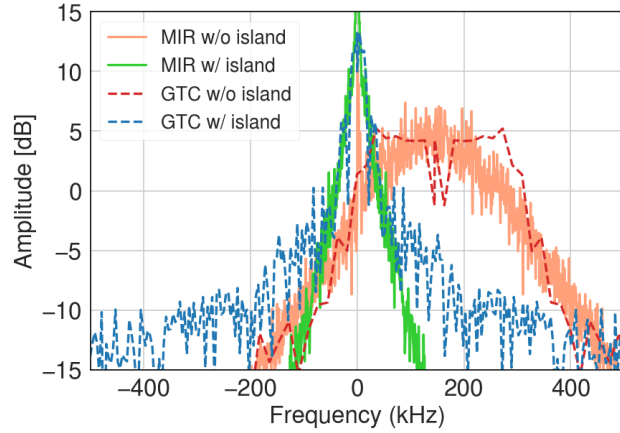


Figure 13 Comparison of turbulence frequency spectrum between MIR measurement of KSTAR discharge #19115 and GTC simulation. Dashed lines are from simulation (labeled as 'GTC') and solid lines are from MIR data (labeled as 'MIR'). The red line has been shifted horizontally to match the rotation frequency of the orange line (rotation frequency). Both the blue line and red line have been shifted vertically to match the peaked amplitude with the MIR measurement.

Table 1 Comparison of the spectrum width in Fig.13.

	With MI	Without MI
MIR spectrum width (kHz)	99.6	19.2
GTC spectrum width(kHz)	99.3	25.2

In addition, we have compared the perpendicular wavenumber  $k_{\perp}$  spectrum between GTC simulation of #19118 and MIR measurement of #19115 in Fig. 14. The results from simulation and experiment agree well. In the case without MI, the turbulence is driven by ITG instability and the  $k_{\perp}\rho_i$  spectrum goes through a reverse cascading process in the nonlinear stage and eventually peaked at  $k_{\perp}\rho_i \approx 0.25$ . While in the case with MI, the amplitude of the vortex mode is larger than the ITG turbulence, and the  $k_{\perp}$  is dominated by the  $k_r$  of the vortex mode, which can be estimated from the island width,  $k_r\rho_i \sim \rho_i 2\pi/w_{is} = 0.11$ . Thus the  $k_{\perp}\rho_i$  spectrum with island is much narrower. Note that the dominance of vortex mode does not directly introduce the transport enhancement. The spatial structure of  $Q_i$  and  $Q_e$  in Fig. 10 indicate the transport are mainly driven by turbulence, which is regulated by the zonal flow and vortex flow with the presence of MIs.

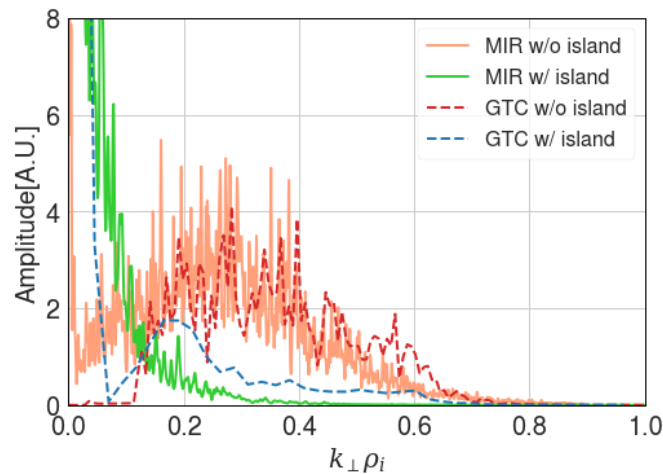


Figure 14 Comparison of  $k_{\perp}\rho_i$  spectrum between MIR measurement of KSTAR discharge #19118 and GTC simulation. Dashed lines are from simulation (labeled as 'GTC') and solid lines are from MIR data (labeled as 'MIR').

## 4 Summary

In this study, we have applied the gyrokinetic approach to investigate the effects of MIs on ITG turbulent transport in the KSTAR tokamak. By utilizing a separated Monte-Carlo stage and a self-consistent turbulence simulation stage, we achieved a flattened profile while maintaining quasi-neutrality in the turbulence simulation. We observed the generation of the  $m=2$ ,  $n=1$  vortex flow from the coupling between GAM and the static MI field. In the presence of MIs, the turbulence potential oscillates at a lower frequency than the ITG frequency in the case without island. MIs enhance the particle and heat transport in both ion and electron channels, which is further modulated by vortex flows and oscillates at the GAM frequency. Zonal flows are predominantly generated outside the island region, with a significant flow shear near the island separatrix. Under the effect of zonal flows and vortex flows, the transport is redistributed spatially. On a poloidal plane, the radial heat transport is concentrated along the island separatrix but also penetrates in the island region via the X-points. Transport along the island separatrix shows toroidal dependence during the vortex flow oscillation. When the vortex flow damps, transport at  $q = 2$  surface is more intense at  $\zeta = \pi$  than  $\zeta = 0$ , where one of the X-points is located at the outer-mid plane (bad curvature region). These findings suggests that the confinement can be improved more efficiently by suppressing the transport near  $q = 2$  and  $\zeta = \pi$ . For the first time, the quantitative agreements between simulations and experiments have been shown on the MI impact of frequency and perpendicular wavenumber spectrum. In the current work, we found the heat transport driven by ITG turbulence is much larger than the particle transport within the island region, which is not consistent with the measurement near the edge. Besides, we only include the  $m=2$ ,  $n=1$  resonant component of  $\delta\mathbf{B}$ . In the future work, we will compare the impact on transport from resonant and non-resonant components. We will include the plasma boundary region to compare the particle transport driven by turbulence and the density pump-out measurement.

## Acknowledgement

We would like to thank T.S. Hahm for useful discussions. This work is supported by US-DOE under grant DE-SC0023434 and DE-FG02-07ER54916, and used resources of the Oak Ridge Leadership Computing Facility at Oak Ridge National Laboratory (DOE Contract No. DE-AC05-00OR22725) through an INCITE award and the National Energy Research Scientific Computing Center (DOE Contract No. DE-AC02-05CH11231). This report was prepared as an account of work sponsored by an agency of the United States Government. Neither the United States Government nor any agency thereof, nor any of their employees, makes any warranty, express or implied, or assumes any legal liability or responsibility for the accuracy, completeness, or usefulness of any information, apparatus, product, or process disclosed, or represents that its use would not infringe privately owned rights. Reference herein to any specific commercial product, process, or service by trade name, trade-mark, manufacturer, or otherwise, does not necessarily constitute or imply its endorsement, recommendation, or favoring by the United States Government or any agency thereof. The views and opinions of authors expressed herein do not necessarily state or reflect those of the United States Government or any agency thereof.

## References

- [1] T. C. Hender *et al.*, “Effect of resonant magnetic perturbations on COMPASS-C tokamak discharges,” *Nucl. Fusion*, vol. 32, no. 12, pp. 2091–2117, Dec. 1992, doi: 10.1088/0029-5515/32/12/102.
- [2] T. E. Evans *et al.*, “Suppression of Large Edge-Localized Modes in High-Confinement DIII-D Plasmas with a Stochastic Magnetic Boundary,” *Phys. Rev. Lett.*, vol. 92, no. 23, p. 235003, Jun. 2004, doi: 10.1103/PhysRevLett.92.235003.
- [3] Y. Liang *et al.*, “Active Control of Type-I Edge-Localized Modes with  $n=1$  Perturbation Fields in the JET Tokamak,” *Phys. Rev. Lett.*, vol. 98, no. 26, p. 265004, Jun. 2007, doi: 10.1103/PhysRevLett.98.265004.
- [4] Y. M. Jeon *et al.*, “Suppression of Edge Localized Modes in High-Confinement KSTAR Plasmas by Nonaxisymmetric Magnetic Perturbations,” *Phys. Rev. Lett.*, vol. 109, no. 3, p. 035004, Jul. 2012, doi: 10.1103/PhysRevLett.109.035004.

- 1  
2  
3 [5] Y. Sun *et al.*, “Nonlinear Transition from Mitigation to Suppression of the Edge Localized Mode with  
4 Resonant Magnetic Perturbations in the EAST Tokamak,” *Phys. Rev. Lett.*, vol. 117, no. 11, p. 115001, Sep.  
5 2016, doi: 10.1103/PhysRevLett.117.115001.
- 6 [6] H. Frerichs *et al.*, “Heuristic predictions of RMP configurations for ELM suppression in ITER burning  
7 plasmas and their impact on divertor performance,” *Nucl. Fusion*, vol. 64, no. 7, p. 076035, Jun. 2024, doi:  
8 10.1088/1741-4326/ad4e47.
- 9 [7] W.-H. Ko *et al.*, “Overview of the KSTAR experiments toward fusion reactor,” *Nucl. Fusion*, 2024, doi:  
10 10.1088/1741-4326/ad3b1d.
- 11 [8] T. E. Evans *et al.*, “Edge stability and transport control with resonant magnetic perturbations in collisionless  
12 tokamak plasmas,” *Nat. Phys.*, vol. 2, no. 6, pp. 419–423, Jun. 2006, doi: 10.1038/nphys312.
- 13 [9] R. B. White, D. A. Monticello, M. N. Rosenbluth, and B. V. Waddell, “Saturation of the tearing mode,” *Phys.*  
14 *Fluids*, vol. 20, no. 5, pp. 800–805, May 1977, doi: 10.1063/1.861939.
- 15 [10] J. W. Connor *et al.*, “A review of internal transport barrier physics for steady-state operation of tokamaks,”  
16 *Nucl. Fusion*, vol. 44, no. 4, p. R1, Mar. 2004, doi: 10.1088/0029-5515/44/4/R01.
- 17 [11] S. Inagaki *et al.*, “Observation of Reduced Heat Transport inside the Magnetic Island O Point in the Large  
18 Helical Device,” *Phys. Rev. Lett.*, vol. 92, no. 5, p. 055002, Feb. 2004, doi: 10.1103/PhysRevLett.92.055002.
- 19 [12] K. Ida and T. Fujita, “Internal transport barrier in tokamak and helical plasmas,” *Plasma Phys. Control.*  
20 *Fusion*, vol. 60, no. 3, p. 033001, Mar. 2018, doi: 10.1088/1361-6587/aa9b03.
- 21 [13] M. J. Choi *et al.*, “Multiscale interaction between a large scale magnetic island and small scale turbulence,”  
22 *Nucl. Fusion*, vol. 57, no. 12, p. 126058, Dec. 2017, doi: 10.1088/1741-4326/aa86fe.
- 23 [14] M. J. Choi *et al.*, “Effects of plasma turbulence on the nonlinear evolution of magnetic island in tokamak,”  
24 *Nat. Commun.*, vol. 12, no. 1, p. 375, Jan. 2021, doi: 10.1038/s41467-020-20652-9.
- 25 [15] K. C. Shaing, “Magnetohydrodynamic-activity-induced toroidal momentum dissipation in collisionless  
26 regimes in tokamaks,” *Phys. Plasmas*, vol. 10, no. 5, pp. 1443–1448, May 2003, doi: 10.1063/1.1567285.
- 27 [16] G. Dong and Z. Lin, “Effects of magnetic islands on bootstrap current in toroidal plasmas,” *Nucl. Fusion*,  
28 vol. 57, no. 3, p. 036009, Mar. 2017, doi: 10.1088/1741-4326/57/3/036009.
- 29 [17] C. J. McDavitt and P. H. Diamond, “Multiscale interaction of a tearing mode with drift wave turbulence: A  
30 minimal self-consistent model,” *Phys. Plasmas*, vol. 13, no. 3, p. 032302, Mar. 2006, doi:  
31 10.1063/1.2177585.
- 32 [18] T. S. Hahm, Y. J. Kim, P. H. Diamond, and G. J. Choi, “Anisotropic  $E \times B$  shearing rate in a magnetic  
33 island,” *Phys. Plasmas*, vol. 28, no. 2, p. 022302, Feb. 2021, doi: 10.1063/5.0036583.
- 34 [19] G. J. Choi and T. S. Hahm, “Long Term Vortex Flow Evolution around a Magnetic Island in Tokamaks,”  
35 *Phys. Rev. Lett.*, vol. 128, no. 22, p. 225001, Jun. 2022, doi: 10.1103/PhysRevLett.128.225001.
- 36 [20] J. Cao, A. Wang, X. Gong, D. Xiang, Q. Huang, and J. Yu, “Kinetic theory of passing energetic ion transport  
37 in presence of the resonant interactions with a rotating magnetic island,” *Phys. Plasmas*, vol. 23, no. 1, p.  
38 012301, Jan. 2016, doi: 10.1063/1.4939084.
- 39 [21] J. Zhao, J. Cao, D. Xiang, Y. Dai, J. Yang, and W. Yang, “Effects of rotating magnetic island on the transport  
40 of trapped fast ions,” *Phys. Plasmas*, vol. 29, no. 8, p. 082502, Aug. 2022, doi: 10.1063/5.0089582.
- 41 [22] H. R. Wilson and J. W. Connor, “The influence of magnetic islands on drift mode stability in magnetized  
42 plasma,” *Plasma Phys. Control. Fusion*, vol. 51, no. 11, p. 115007, Oct. 2009, doi: 10.1088/0741-  
43 3335/51/11/115007.
- 44 [23] A. Ishizawa and P. H. Diamond, “Ion-temperature gradient modes affected by helical magnetic field of  
45 magnetic islands,” *Phys. Plasmas*, vol. 17, no. 7, p. 074503, Jul. 2010, doi: 10.1063/1.3460346.
- 46 [24] W. A. Hornsby *et al.*, “The non-linear evolution of the tearing mode in electromagnetic turbulence using  
47 gyrokinetic simulations,” *Plasma Phys. Control. Fusion*, vol. 58, no. 1, p. 014028, Jan. 2016, doi:  
48 10.1088/0741-3335/58/1/014028.
- 49 [25] Z. X. Wang, J. Q. Li, J. Q. Dong, and Y. Kishimoto, “Generic Mechanism of Microturbulence Suppression  
50 by Vortex Flows,” *Phys. Rev. Lett.*, vol. 103, no. 1, p. 015004, Jul. 2009, doi:  
51 10.1103/PhysRevLett.103.015004.
- 52 [26] J.-M. Kwon *et al.*, “Gyrokinetic simulation study of magnetic island effects on neoclassical physics and  
53 micro-instabilities in a realistic KSTAR plasma,” *Phys. Plasmas*, vol. 25, no. 5, p. 052506, May 2018, doi:  
54 10.1063/1.5027622.
- 55  
56  
57  
58  
59  
60



- 1  
2  
3 [27] F. Wang, J. Li, H. Qu, and X. Peng, "Gyrokinetic simulation of magnetic-island-induced electric potential  
4 vortex mode," *Plasma Sci. Technol.*, vol. 26, no. 1, p. 015103, Jan. 2024, doi: 10.1088/2058-6272/ad0d57.
- 5 [28] D. Zarzoso, W. A. Hornsby, E. Poli, F. J. Casson, A. G. Peeters, and S. Nasr, "Impact of rotating magnetic  
6 islands on density profile flattening and turbulent transport," *Nucl. Fusion*, vol. 55, no. 11, p. 113018, Sep.  
7 2015, doi: 10.1088/0029-5515/55/11/113018.
- 8 [29] O. Izacard, C. Holland, S. D. James, and D. P. Brennan, "Dynamics of ion temperature gradient turbulence  
9 and transport with a static magnetic island," *Phys. Plasmas*, vol. 23, no. 2, p. 022304, Feb. 2016, doi:  
10 10.1063/1.4941704.
- 11 [30] A. B. Navarro, L. Bardóczi, T. A. Carter, F. Jenko, and T. L. Rhodes, "Effect of magnetic islands on profiles,  
12 flows, turbulence and transport in nonlinear gyrokinetic simulations," *Plasma Phys. Control. Fusion*, vol.  
13 59, no. 3, p. 034004, Mar. 2017, doi: 10.1088/1361-6587/aa557e.
- 14 [31] F. Hariri, P. Hill, M. Ottaviani, and Y. Sarazin, "Plasma turbulence simulations with X-points using the  
15 flux-coordinate independent approach," *Plasma Phys. Control. Fusion*, vol. 57, no. 5, p. 054001, May 2015,  
16 doi: 10.1088/0741-3335/57/5/054001.
- 17 [32] P. Hill, F. Hariri, and M. Ottaviani, "The effect of magnetic islands on Ion Temperature Gradient turbulence  
18 driven transport," *Phys. Plasmas*, vol. 22, no. 4, p. 042308, Apr. 2015, doi: 10.1063/1.4919031.
- 19 [33] Q. M. Hu *et al.*, "The density dependence of edge-localized-mode suppression and pump-out by resonant  
20 magnetic perturbations in the DIII-D tokamak," *Phys. Plasmas*, vol. 26, no. 12, p. 120702, Dec. 2019, doi:  
21 10.1063/1.5134767.
- 22 [34] S. K. Kim *et al.*, "Transition in particle transport under resonant magnetic perturbations in a tokamak," *Nucl.*  
23 *Fusion*, vol. 63, no. 10, p. 106013, Oct. 2023, doi: 10.1088/1741-4326/acef3c.
- 24 [35] A. Ishizawa, Y. Kishimoto, and Y. Nakamura, "Multi-scale interactions between turbulence and magnetic  
25 islands and parity mixture—a review," *Plasma Phys. Control. Fusion*, vol. 61, no. 5, p. 054006, May 2019,  
26 doi: 10.1088/1361-6587/ab06a8.
- 27 [36] M. J. Choi, "Interaction between a magnetic island and turbulence," *Rev. Mod. Plasma Phys.*, vol. 5, no. 1,  
28 p. 9, Nov. 2021, doi: 10.1007/s41614-021-00058-w.
- 29 [37] Z. Lin, T. S. Hahm, W. W. Lee, W. M. Tang, and R. B. White, "Turbulent Transport Reduction by Zonal  
30 Flows: Massively Parallel Simulations," *Science*, vol. 281, no. 5384, pp. 1835–1837, Sep. 1998, doi:  
31 10.1126/science.281.5384.1835.
- 32 [38] H. Y. Wang *et al.*, "Global gyrokinetic particle simulations of microturbulence in W7-X and LHD  
33 stellarators," *Phys. Plasmas*, vol. 27, no. 8, p. 082305, Aug. 2020, doi: 10.1063/5.0014198.
- 34 [39] W. H. Wang, X. S. Wei, Z. Lin, C. Lau, S. Dettrick, and T. Tajima, "A gyrokinetic simulation model for 2D  
35 equilibrium potential in the scrape-off layer of a field-reversed configuration," *Phys. Plasmas*, vol. 31, no.  
36 7, p. 072507, Jul. 2024, doi: 10.1063/5.0189761.
- 37 [40] Y. Xiao and Z. Lin, "Turbulent Transport of Trapped-Electron Modes in Collisionless Plasmas," *Phys. Rev.*  
38 *Lett.*, vol. 103, no. 8, p. 085004, Aug. 2009, doi: 10.1103/PhysRevLett.103.085004.
- 39 [41] P. Liu *et al.*, "Regulation of Alfvén Eigenmodes by Microturbulence in Fusion Plasmas," *Phys. Rev. Lett.*,  
40 vol. 128, no. 18, p. 185001, May 2022, doi: 10.1103/PhysRevLett.128.185001.
- 41 [42] G. Brochard *et al.*, "Saturation of Fishbone Instability by Self-Generated Zonal Flows in Tokamak Plasmas,"  
42 *Phys. Rev. Lett.*, vol. 132, no. 7, p. 075101, Feb. 2024, doi: 10.1103/PhysRevLett.132.075101.
- 43 [43] P. Jiang, Z. Lin, I. Holod, and C. Xiao, "Effects of magnetic islands on drift wave instability," *Phys. Plasmas*,  
44 vol. 21, no. 12, p. 122513, Dec. 2014, doi: 10.1063/1.4903910.
- 45 [44] D. Liu, W. Zhang, J. McClenaghan, J. Wang, and Z. Lin, "Verification of gyrokinetic particle simulation of  
46 current-driven instability in fusion plasmas. II. Resistive tearing mode," *Phys. Plasmas*, vol. 21, no. 12, p.  
47 122520, Dec. 2014, doi: 10.1063/1.4905074.
- 48 [45] D. Liu, J. Bao, T. Han, J. Wang, and Z. Lin, "Verification of gyrokinetic particle simulation of current-  
49 driven instability in fusion plasmas. III. Collisionless tearing mode," *Phys. Plasmas*, vol. 23, no. 2, p.  
50 022502, Feb. 2016, doi: 10.1063/1.4941094.
- 51 [46] J. C. Li, C. J. Xiao, Z. H. Lin, and K. J. Wang, "Effects of electron cyclotron current drive on magnetic  
52 islands in tokamak plasmas," *Phys. Plasmas*, vol. 24, no. 8, p. 082508, Aug. 2017, doi: 10.1063/1.4996021.
- 53 [47] J. Li, C. Xiao, Z. Lin, D. Liu, X. Ji, and X. Wang, "GTC simulation of linear stability of tearing mode and  
54 a model magnetic island stabilization by ECCD in toroidal plasma," *Phys. Plasmas*, vol. 27, no. 4, p. 042507,  
55 Apr. 2020, doi: 10.1063/1.511127.
- 56  
57  
58  
59  
60

- 1  
2  
3 [48] K. S. Fang and Z. Lin, “Global gyrokinetic simulation of microturbulence with kinetic electrons in the  
4 presence of magnetic island in tokamak,” *Phys. Plasmas*, vol. 26, no. 5, p. 052510, May 2019, doi:  
5 10.1063/1.5096962.
- 6 [49] K. FANG, J. BAO, and Z. LIN, “Gyrokinetic simulations of nonlinear interactions between magnetic islands  
7 and microturbulence,” *Plasma Sci. Technol.*, vol. 21, no. 11, p. 115102, Sep. 2019, doi: 10.1088/2058-  
8 6272/ab3c83.
- 9 [50] H. Shi *et al.*, “Verification of gyrokinetic particle simulation of current-driven instability in fusion plasmas.  
10 IV. Drift-tearing mode,” *Phys. Plasmas*, vol. 26, no. 9, p. 092512, Sep. 2019, doi: 10.1063/1.5116332.
- 11 [51] H. Shi *et al.*, “Temperature Gradient, Toroidal and Ion FLR Effects on Drift-Tearing Modes\*,” *Chin. Phys.*  
12 *Lett.*, vol. 37, no. 8, p. 085201, Aug. 2020, doi: 10.1088/0256-307X/37/8/085201.
- 13 [52] Y. Yao, Z. Lin, J. Q. Dong, P. Shi, S. F. Liu, and J. Li, “Gyrokinetic simulations of double tearing modes  
14 in toroidal plasma,” *Phys. Lett. A*, vol. 417, p. 127681, Nov. 2021, doi: 10.1016/j.physleta.2021.127681.
- 15 [53] X. Tang *et al.*, “Gyrokinetic particle simulations of interactions between energetic particles and magnetic  
16 islands induced by neoclassical tearing modes,” *Phys. Plasmas*, vol. 27, no. 3, p. 032508, Mar. 2020, doi:  
17 10.1063/1.5126681.
- 18 [54] J. Li *et al.*, “Global gyrokinetic simulations of the impact of magnetic island on ion temperature gradient  
19 driven turbulence,” *Nucl. Fusion*, vol. 63, no. 9, p. 096005, Sep. 2023, doi: 10.1088/1741-4326/ace461.
- 20 [55] K. Wang *et al.*, “Verification of gyrokinetic particle simulations of neoclassical tearing modes in fusion  
21 plasmas,” *Plasma Phys. Control. Fusion*, vol. 65, no. 10, p. 105005, Aug. 2023, doi: 10.1088/1361-  
22 6587/aceb88.
- 23 [56] I. Holod, Z. Lin, S. Taimourzadeh, R. Nazikian, D. Spong, and A. Wingen, “Effect of resonant magnetic  
24 perturbations on microturbulence in DIII-D pedestal,” *Nucl. Fusion*, vol. 57, no. 1, p. 016005, Oct. 2016,  
25 doi: 10.1088/0029-5515/57/1/016005.
- 26 [57] S. Taimourzadeh, L. Shi, Z. Lin, R. Nazikian, I. Holod, and D. Spong, “Effects of RMP-induced changes of  
27 radial electric fields on microturbulence in DIII-D pedestal top,” *Nucl. Fusion*, vol. 59, no. 4, p. 046005,  
28 Apr. 2019, doi: 10.1088/1741-4326/aafe3a.
- 29 [58] J. FU, P. LIU, X. WEI, Z. LIN, N. M. FERRARO, and R. NAZIKIAN, “Effects of resonant magnetic  
30 perturbations on radial electric fields in DIII-D tokamak,” *Plasma Sci. Technol.*, vol. 23, no. 10, p. 105104,  
31 Aug. 2021, doi: 10.1088/2058-6272/ac190e.
- 32 [59] S. M. Yang *et al.*, “Nonambipolar Transport due to Electrons with 3D Resistive Response in the KSTAR  
33 Tokamak,” *Phys. Rev. Lett.*, vol. 123, no. 9, p. 095001, Aug. 2019, doi: 10.1103/PhysRevLett.123.095001.
- 34 [60] L. Bardóczi *et al.*, “Modulation of Core Turbulent Density Fluctuations by Large-Scale Neoclassical  
35 Tearing Mode Islands in the DIII-D Tokamak,” *Phys. Rev. Lett.*, vol. 116, no. 21, p. 215001, May 2016, doi:  
36 10.1103/PhysRevLett.116.215001.
- 37 [61] S. Lippmann, M. Finkenthal, H. W. Moos, S. C. McCool, and A. J. Wootton, “Effects of an ergodic magnetic  
38 limiter on the edge plasma properties of the TEXT tokamak,” *Nucl. Fusion*, vol. 31, no. 11, pp. 2131–2140,  
39 Nov. 1991, doi: 10.1088/0029-5515/31/11/009.
- 40 [62] S. C. Jardin, “A triangular finite element with first-derivative continuity applied to fusion MHD  
41 applications,” *J. Comput. Phys.*, vol. 200, no. 1, pp. 133–152, Oct. 2004, doi: 10.1016/j.jcp.2004.04.004.
- 42 [63] W. LEE, “GYROKINETIC PARTICLE SIMULATION-MODEL,” *J. Comput. Phys.*, vol. 72, no. 1, pp.  
43 243–269, Sep. 1987, doi: 10.1016/0021-9991(87)90080-5.
- 44 [64] Z. LIN and W. LEE, “METHOD FOR SOLVING THE GYROKINETIC POISSON EQUATION IN  
45 GENERAL GEOMETRY,” *Phys. Rev. E*, vol. 52, no. 5, B, pp. 5646–5652, Nov. 1995, doi:  
46 10.1103/PhysRevE.52.5646.
- 47 [65] Z. Lin, Y. Nishimura, Y. Xiao, I. Holod, W. L. Zhang, and L. Chen, “Global gyrokinetic particle simulations  
48 with kinetic electrons,” *Plasma Phys. Control. Fusion*, vol. 49, no. 12B, p. B163, Nov. 2007, doi:  
49 10.1088/0741-3335/49/12B/S15.
- 50 [66] I. Holod, W. L. Zhang, Y. Xiao, and Z. Lin, “Electromagnetic formulation of global gyrokinetic particle  
51 simulation in toroidal geometry,” *Phys. Plasmas*, vol. 16, no. 12, p. 122307, Dec. 2009, doi:  
52 10.1063/1.3273070.
- 53 [67] T. Hahm, Z. Lin, W. Lee, and W. Tang, “Reduction of turbulence by zonal flows,” in *THEORY OF FUSION*  
54 *PLASMAS*, J. Connor, E. Sindoni, and J. Vaclavik, Eds., in INTERNATIONAL SCHOOL OF PLASMA  
55 PHYSICS - PIERO CALDIROLA, vol. 18. Univ Milano, Dept Fis; Inst Fis Plasma CNR, Milano; Int Sch  
56  
57  
58  
59  
60

1  
2  
3 Plasma Phys, Piero Caldirola; Ctr Rech Phys Plasmas, Ecole Polytech Fed Lausanne, Assoc Euratom Suisse;  
4 Adm Provinciale Lecco; Commiss European Comm (CEC-EURATOM), Brussels, Belgium; Entr Nuove  
5 Tecnol, Energia Ambiente (ENEA); Camera Commercio lecco; Ctr Innovaz Lecco SPA., 1999, pp. 443–  
6 448.

7 [68] W. Lee *et al.*, “Microwave imaging reflectometry for density fluctuation measurement on KSTAR,” *Nucl*  
8 *Fusion*, 2014.

9 [69] W. Lee *et al.*, “Quasi-coherent fluctuation measurement with the upgraded microwave imaging  
10 reflectometer in KSTAR,” *Plasma Phys. Control. Fusion*, vol. 60, no. 11, p. 115009, Oct. 2018, doi:  
11 10.1088/1361-6587/aae0b5.  
12  
13  
14  
15  
16  
17  
18  
19  
20  
21  
22  
23  
24  
25  
26  
27  
28  
29  
30  
31  
32  
33  
34  
35  
36  
37  
38  
39  
40  
41  
42  
43  
44  
45  
46  
47  
48  
49  
50  
51  
52  
53  
54  
55  
56  
57  
58  
59  
60